Pink beam far-field imaging of micropipes and voids in SiC: a quantitative approach

T. S. Argunova[1], V. G. Kohn[2], M. Yu. Gutkin[3,4,5], J. H. Lim[6] and J. H. Je[7,*]

[1] Ioffe Physico-Technical Institute RAS, 194021 St. Petersburg, Russia
[2] National Research Center "Kurchatov Institute", 123182 Moscow, Russia
[3] Institute of Problems in Mechanical Engineering RAS, 199178 St. Petersburg, Russia
[4] Department of Mechanics and Control Processes, St. Petersburg State Polytechnical University, 195251 St. Petersburg, Russia
[5] Department of LED Technologies, ITMO University, 197101 St. Petersburg, Russia
[6] Beamline division, Pohang Accelerator Laboratory, 790-784 Pohang, Republic of Korea
[7] Department of Materials Science and Engineering, Pohang University of Science and Technology, 790-784 Pohang, Republic of Korea

Quantitative analysis methods of pink beam synchrotron radiation phase contrast images are presented. The contrasts of micro-objects are weak in the near field but increase in the far field. However, the sizes of the object images in the far field are different from the real objects sizes; therefore computer simulations are needed to accurately retrieve the objects sizes. We first describe the basics of the simulations, in particular, for micro-objects such as micropipes in silicon carbide single crystals. Then we apply computer simulations to the cross section size and shape measurements of the micropipes, one-dimensional (1D) objects. In case of aligning the micropipe axis normal to the beam, our Fit Micro-Tube Image (FIMTIM) program allows us to obtain the solution automatically. We also discuss the limitations of this approach by revealing the changes in shapes and sizes of the micropipes. A theoretical model which describes the origin of the changes is suggested. Finally we demonstrate the simulations of 2D spherical micro-voids and compare them with experimental images. Pink beam far-field imaging is an effective approach for visualizing micro-objects inside absorbing solids and our quantitative analysis methods based on computer simulations can be a general framework for precise measurement of micro-object sizes.

Keywords: crystal structure; defects; synchrotron radiation; x-ray scattering; phase contrast; imaging; micropipe; silicon carbide

1. Introduction

Third generation synchrotron radiation (SR) sources allow one to obtain x-ray phase contrast images even using x-ray beams with low [1, 2] monochromaticity. In particular, high flux of polychromatic pink SR permits to visualize internal microstructures of highly absorbing solids [3]. The simple in-line scheme quite sensitively reveals micro scale inclusions, voids, cracks and other inhomogeneities which can exist in advanced electronic materials [4-6]. Microscopic tubular pores or micropipes are of particular interest in research domains of bulk silicon carbide (SiC) [7-9]. The micropipe diameters in SiC vary from a few tenths to a few tens of micrometers [7-9]. Investigation of the micropipe shapes and sizes in correlation with crystal growth parameters is an important problem that needs to be solved for understanding their nature and eventually for the production of low-cost high-quality crystals.

Phase contrast imaging is known to require a high degree of spatial coherence. In 3rd generation SR sources, the spatial coherence is already provided by their small angular sizes. As a rule, temporal coherence is formed by the applied monochromator. However, we note that a SR spectrum is reducible to a peak with a maximum intensity at certain energy even without using a monochromator [2]. First of all, the radiation intensity decreases with energy in high energy regions owing to limited electron beam energy. On the other hand, low energies are preferentially absorbed when the beam passes through all the absorbers on its path, including the sample itself. The two effects result in a broad spectral peak centered on a certain energy, as demonstrated in Fig. 1(a) for Pohang Light Source (PLS) in Korea, a medium-brilliant SR source. Here, based on the absorption by a SiC plate of 490 μm thick, a spectral peak with the maximum energy $E = 16$ keV and an effective full width at half maximum (FWHM) $\Delta E \approx 24$ keV was obtained. As an absorbing material, a thick sample itself may be sufficient, but the absorption, if the sample is too thin, can be enhanced by adding an absorber.

Coherence for nonmonochromatic beams can be characterized by temporal and spatial coherence lengths. The temporal coherence length L_t is determined by the FWHM ΔE, or $\Delta\lambda$ [10, 11]: $L_t = hc/\Delta E = \lambda^2/\Delta\lambda$, where h is the Planck constant and c is the speed of light. For the wavelength at the maximum peak with the SiC absorber $\lambda = 0.775$ Å ($E = 16$ keV), and the FWHM $\Delta\lambda = 0.52$ Å in Fig. 1(a), the temporal coherence length is estimated as $L_t = 1.2$ Å. The temporal coherence length, though small, is quite enough to form the interference patterns in the central part of the image. On the other hand, the spatial coherence length L_s is estimated as $L_s = \lambda/\alpha = 42$ μm, where $\alpha = S/z_0$ is the angular size at the source-to-sample distance z_0 (32 m) for the vertical source size $S = 60$ μm. The spatial coherence length is much larger than typical micropipe diameters.

For a micropipe of 1 μm in diameter (D) the phase shift is small and thus the phase contrast is weak. If the sample-to-detector distance z_1 is small (a near field), the radius of the first Fresnel zone $r_1 = (\lambda z_1)^{1/2}$ can be smaller than D. The image size, which is nearly equal to the object size, is too small to be detected with the poor detector resolution of typical pixel sizes about 1 μm. As z_1 increases, the contrast becomes stronger and the image size is gradually enlarged at the same time, enabling one to visualize the micropipes with typical detectors. In that sense, the far field (where $r_1 > D$) is appropriate for investigating the micropipes.

In this work we present a quantitative approach to phase contrast imaging of micropipes and micro-voids in SiC crystals. We show how the phase contrast theory is used in a computer program to simulate the images of the micropipes and determine their cross sections. We also discuss the nature of investigated micropipes. We shortly review our results to demonstrate the basic rules of image formation in pink SR. Finally, simulations of 2D micro-object images of spherical voids as an example are demonstrated.
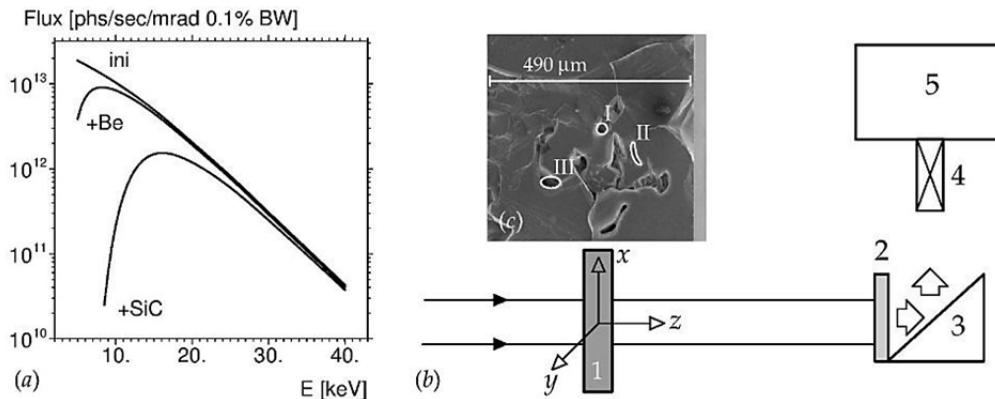
Fig. 1 (a) A spectrum of the pink SR beam at PLS. The upper curve is an initial spectrum. The middle curve is an effective spectrum after a passage of 2 mm thick Be window. The lower curve is an effective spectrum behind the 490 μm thick SiC plate. (b) Experimental scheme: 1 - sample; 2 - scintillator (150 μm thick); 3 - mirror; 4 - objective; 5 -detector. SR beam is parallel to the z axis. Micropipes are mostly parallel to y axis. The distance between the scintillator and the sample z_1 was varied from 10 to 45 cm. (c) SEM cross-section image of the 4H-SiC wafer of 490 μm thickness. Opening of micropipes is seen as hexagonal (I), slit-like (II), or elliptical (III) etch-pits.

2. Experimental procedure

Several slices (~ 500 μm thick) were axially cut along the growth direction [0001] of sublimation grown [12] 4H and 6H SiC boules that contain voids and micropipes. The (0001) SiC plates were mechanically and chemically mirror-polished on both sides to remove a damage layer and a surface roughness.

Imaging experiments were carried out at 6D x-ray micro-imaging beamline in PLS. The experimental setup is shown in Fig. 1(b). The polychromatic radiation was extracted from a bending magnet port located at a distance of 32 m from a sample. The source size was 160 μm × 60 μm (H × V). After passing through a slit in front of the hutch, the radiation arrives at the sample 1 (Fig. 1(b)). Once penetrating the sample, the polychromatic radiation changes to a pink beam as seen in Fig. 1(a). The pink beam x-ray image is converted into visible image by the scintillator (CdWO$_4$ crystal) 2, which is then reflected from a polished silicon mirror 3 and reaches the detector 5 after 20× magnified by the optical objective 4.

The [0001] direction of the sample plate was aligned parallel to the y-axis direction and perpendicular to the beam direction (the z-direction) (Fig. 1(b)). Then the micropipes that are almost in parallel to the [0001] direction are approximately in the y-direction and their images are obtained in a more coherent vertical direction (x-axis). The scanning electron microscopy (SEM) image in Fig. 1(c) shows the cross-section of the sample plate with 490 μm thickness. One can see hexagonal (I), slit-like (II), or elliptical (III) pores on the etched surface.

By virtue of the high flux pink SR beam, thick SiC samples can be imaged with short exposure times of a few milliseconds. However, because of parasitic scattering by a statistical noise of the source (SNS) and an inhomogeneous scintillation, *etc.*, it is required to get substantially high signals comparing to background. The signal-to-SNS ratio is defined as $C/2N^{1/2}$, where C is a contrast and N is a maximal count rate (intensity). The contrast C is equal to the difference between the maximal and the minimal intensities of the image divided by the sum of these values; therefore the exposure time should be a maximal possible value to provide sufficiently high intensity. For two CCD detectors M_1 and M_2 of 12 and 14 bit dynamic ranges, respectively, suppose $N_1 = 3200$ and $N_2 = 12000$ photons per second, and $C_1 = 550$ and $C_2 = 3000$ photons. Then the signal-to-SNS ratios become 5 and 14 for M_1 and M_2, respectively, suggesting the preference for M_2 CCD with the higher count rate.

Apart from the signal-to-SNS ratio, one has to take care of CCD matrix pixel size. We notice that image quality is influenced by the pixel-to-object size ratio rather than the pixel size alone. In the near field the image size of a

micropipe is nearly equal to its diameter D (~a few μm). Then the pixel size determines the resolution. In this respect, CCD M_1 with 5.5 μm×5.5 μm pixel size is preferred to CCD M_2 with 9 μm×9 μm one. The pixel-to-object size ratio can be reduced using a magnifying optical objective. For example, 20× magnification effectively reduces the above mentioned pixel sizes down to 0.27 μm and 0.45 μm for M_1 and M_2, respectively. However, computer simulation demonstrates that real detector resolution is worse than the pixel size, presumably due to the scintillator parameters, such as the thickness, the efficiency, *etc*. On the other hand, in the far field the image size becomes larger and the pixel size becomes less critical.

What will be the minimal micropipe size that could be measured in the in-line scheme of Fig. 1(b)? Let us consider the most prominent part of the micropipe image which has the bright contrast in its center. The contrast C is proportional to the phase shift with a numerical coefficient close to unity based on computer simulations of various monochromatic images in the Fresnel region [13]. The phase shift is equal to $\varphi = 2\pi\delta t/\lambda$, where λ is the wavelength of a monochromatic SR and t is the object size along the beam. By substituting the decrement of refraction index $\delta = a\lambda^2$, where a is proportional to the electron density of the medium ρ, $\varphi = 2\pi a\lambda t$.

The minimal micropipe size thus depends on both λ and ρ, and specifically increases with the decreases of λ and ρ. For example, when $\varphi = 0.02$, $\lambda = 0.775$ Å and ρ(SiC) $= 3.21$ g/cm^3, one has $a = 4.35\times10^{-6}$ Å^{-2}. Then, the minimal object thickness is estimated as $t = 0.09$ μm. In [14, 15] we obtained the formula for the relative intensity deviation from unity in the center of the bright part of micropipe image C_0 (approximately $C/2$): $C_0 = (\pi^2/2^{1/2})a\lambda(D/r_1)D_0$, where r_1 is the radius of the first Fresnel zone, λ is the wavelength in the spectrum maximum (Fig. 1(a)), D and $D_0 = t$ are the transverse and the longitudinal micropipe diameters.

One can easily see that C_0 is proportional to φ with the coefficient equal to $(\pi/2^{3/2})(D/r_1) = 1.1(D/r_1)$. In the Fresnel region $D/r_1 \approx 1$ and the both C_0 and φ parameters have nearly equal values. In the far field, where $D < r_1$, the contrast weakens.

In fact, the estimation of the longitudinal diameter depends on the contrast which can be experimentally measured. If the contrast $C_0 = 0.02$, then SNS is assumed to be less than 0.02, and therefore more than 2500 photons are measured. However, the noise can be higher for several reasons. The contrast should be at least 4 times larger than the noise. Then the minimal longitudinal diameter enlarges up to $D_0 \approx 0.36$ μm. We note that all setup components produce noise, besides the SR source.

Finally, we consider the influence of the parasitic noise on the image fine structure. We return to the detectors M_1 and M_2 to evaluate their view fields as follows. The M_1 and M_2 resolutions are equal to 3296×2472 and 4008×2672 (H×V) pixels, respectively. For the effective pixel size of 0.27 μm for M_1 and 0.45 μm for M_2, their view fields are 906 μm × 680 μm and 1804 μm × 1202 μm, respectively. The image of the horizontal micropipe of 2 μm in diameter at the sample-to- detector distance 40 cm ($r_1 = 5.5$ μm) does not exceed 30 μm in width. It occupies 4.4% (2.5%) of the M_1 (M_2) view field in the vertical direction, indicating that the quality provided by M_2 is more badly affected by the beam, the scintillator and the optical objective.

In summary, a brief analysis of the instrumental aspects shows that the fine structure of micropipe image in the pink beam can be observed by enhancing the intensity and the pixel-to-object size ratio, and by keeping off large area sensors. Reduced noise allows one to resolve the micropipes even with a longitudinal diameter ≥ 0.1 μm.

3. Basics of computer simulating phase contrast images of micropipes

The intensity profile across a micropipe axis and the beam direction is described by the formula:

$$I(x) = \left|a(x_0)\right|^2, \; a(x) = \int dx_1 P(x - x_1, Z)\, T(x_1) \tag{1}$$

where $x_0 = xz_0/z_t$, $z_t = z_0 + z_1$; and $Z = z_0 z_1/z_t$. The formula is derived under the following approximations: (i) the micropipe is considered as a quasilinear object whose electron density undergoes fast and slow changes along x and along y axes, respectively (see Fig. 1(b) for the axes): this allows us to neglect the intensity variation along the y-axis; (ii) transmission of the radiation through the object is taken into account in the limits of geometrical optics with an additional simplification that all rays are parallel to the z-axis.

Under these assumptions the problem is reduced to the convolution of the Fresnel propagator $P(x,z)$ [16] and the transmission function $T(x)$ where

$$P(x,z) = (i\lambda z)^{-1/2} \exp\left(i\pi \frac{x^2}{\lambda z}\right), \quad T(x) = \exp\left[(i\Phi + M)\left(1 - \frac{x^2}{R^2}\right)^{1/2}\right], \tag{2}$$

Here $\Phi = (4\pi/\lambda)\delta R_0$, $M = \Phi\beta/\delta$, $2R = D$ and $2R_0 = D_0$ are the micropipe diameters across and along the beam, respectively; $\delta - i\beta = 1 - n$, where n is the complex refractive index of the matter. It is assumed that the square root is equal to zero for negative argument.

Since the integrand in (1) does not decay at infinity, for numerical calculations the integral should be rewritten, using the propagator normalization property, in the form

$$a(x) = 1 + \int dx_1 P(x - x_1, Z)[T(x_1) - 1] \qquad (3)$$

Computer simulations were performed with the FIMTIM (Fit Micro-Tube Image) computer program which is elaborated in Java on the base of the formulae (1) - (3) [2, 17, 18]. The program allows: (a) Calculation of monochromatic image profile along the x-axis for a micropipe; (b) Estimation of the real spectrum taking into account all absorbers on the beam path, including the sample itself; (c) Summation of many monochromatic images with the weights following from the spectrum to simulate pink beam image [19] (d) Fitting of the experimental intensity profile to find the transverse D and longitudinal D_0 diameters of micropipe cross-section, i.e. normal and parallel to the beam; (e) Determination and mapping of the dependence of the least square sum $\chi^2(D, D_0)$; (f) Evaluation of accuracy of the obtained parameters.

In addition, the theoretical intensity profile across the micropipe is calculated as a convolution of the source brightness within its size (Gaussian distribution) and the image for a point source. The FWHM of the Gaussian is equal to $S_d = S z_1/z_0$, where S is the effective transverse (vertical) source size. The summation over the spectrum is performed on the set of energy points from 5 to 40 keV with a step of 1 keV.

The program reads the experimental profile of intensity (EPI) and calculates the theoretical profiles (TPI) for predetermined parameters D and D_0 which are called TD (transverse diameter) and LD (longitudinal diameter). Each time EPI is normalized from the condition of better coincidence with TPI. By means of varying the parameters D and D_0 the program automatically searches for a nearest minimum of least square sum $\chi^2(D, D_0)$ on some set of points with a definite steps using an effective algorithm. Starting from big steps for D and D_0 at the beginning, one may sequentially reduce them to increase the accuracy of the minimum point. On the next stage the full minimum region in the plane of parameters D and D_0 is identified with an intelligent algorithm to shorten the calculating time.

The important question for us is a level of accuracy of the obtained values. It is the reason why it is very important to examine the curves $\chi^2 - \chi^2_{min} = B$ with various values of B. The program FIMTIM can draw two-dimensional map of $\chi^2 - \chi^2_{min}$ as a function of D and D_0 near the minimum point [20].

4. Computer simulations

4.1 Computer simulation of micropipe cross sections

With a large view field several micropipes can be recorded simultaneously. Taking into account micropipes that are deviated from the growth direction the images were recorded after adjusting the sample to have the axes of a chosen group of pipes aligned in horizontal positions as can as possible. The images were opened by means of the computer program ImageJ [21]. The intensity profiles were recorded across each pipe axis in the form of numerical arrays. Two or three pixels along the axes could be summed to increase the signal-to-noise ratio. These profiles were used for the simulation.

Figure 2(a) shows a fragment of pink SR phase contrast image of a micropipe in SiC. The sample-to-detector distance is 40 cm. The normalized experimental curve (markers) (obtained from the image) is presented in Fig. 2(b). The maximal experimental intensity or the count rate is equal to $N = 11250$ sec^{-1}; the contrast in photons is $C = 7000$ and the signal-to-noise ratio is 16.5. The best coincidence ($\chi^2 = 9.8 \times 10^{-5}$) with the calculated profile (solid line) was reached for the values of diameters $D = 1.36$ μm and $D_0 = 1.82$ μm.

To estimate the level of accuracy of the obtained diameters the program has drawn the 2D map of $\chi^2 - \chi^2_{min}$ as a function of D and D_0 near the minimum point (Fig. 2(c)). On the map the black and the white colors display $\chi^2_{min} = 9.8 \times 10^{-5}$ and $\chi^2_{max} = 1.13 \times 10^{-4}$, respectively. All the values $\chi^2 > \chi^2_{max}$ were replaced by χ^2_{max}. One can see that the area of small χ^2 values is not localized. It has a minimal dimension along the direction $D = D_0$ and a maximal dimension along the perpendicular direction.

The map demonstrates a universal shape of micropipe image profile in the far field, as first described by Kohn *et al.* [14, 15]. Experiments showed that the change of micropipe cross section size affected not the image size but the contrast. This result is explained by Fraunhofer diffraction in phase objects having small sizes along the beam, when the phase shift $\Delta\varphi < 1$. Estimation shows that $\Delta\varphi < 1/2$ at $\lambda = 0.775$ Å for SiC when $D_0 \leq 2.5$ μm. Fraunhofer diffraction condition for micropipes is satisfied when $D < r_1$, which agrees with the experiment: at $z_1 = 40$ cm the diameter of the first Fresnel zone is $r_1 = 11$ μm.

Under the Fraunhofer diffraction condition the calculated intensity of monochromatic radiation in the central part of the image is determined by the product DD_0, hence by the cross section area. This part is influenced weakly by the pink beam. When the distance increases from the center, oscillations of monochromatic harmonics change which cause a sharp decrease in the total pink beam contrast. In fact only the first oscillations remain, while the others are damped. It is of interest that the central maximums of intensity profiles for all frequencies are proportional to the cross section area.

One can obtain a universal profile by summing up all the monochromatic profiles (for a specific spectrum) divided by the cross section area. In the pink beam such universal profile has only the central peak with strongly damped side oscillations formed by a minimum and a maximum. Some researchers may be tempted to determine the object size from the bright stripe size in the center between the dark stripes. However, it is wrong. This size is in fact the size of the first Fresnel zone.
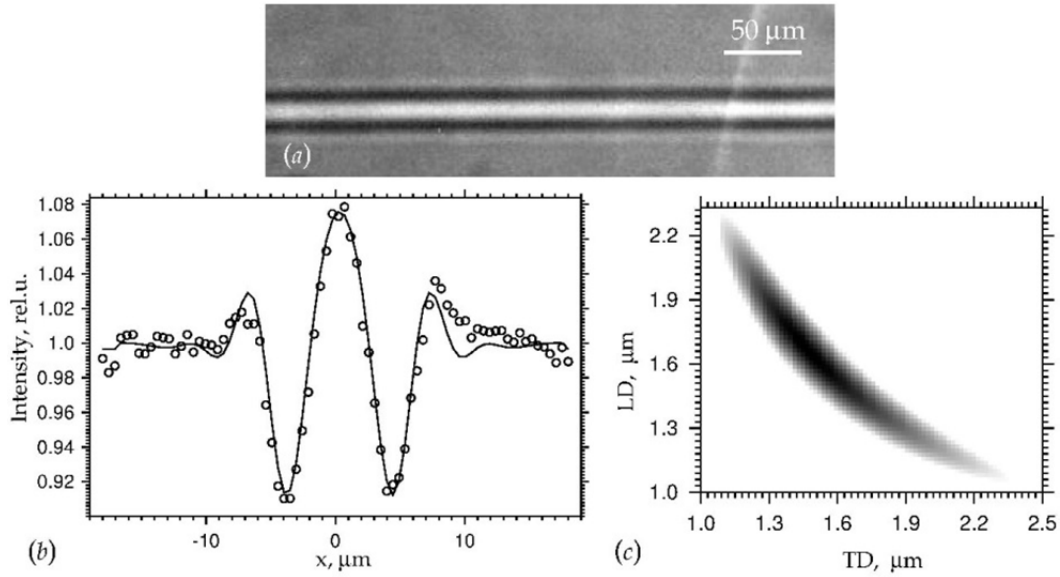
Fig. 2 (a) A micropipe image at 40 cm from the detector. (b) Experimental data and simulated theoretical profile in the case of best coincidence (χ^2=9.8×10^{-5}). (c) A map showing the least square sum χ^2 as a function of D and D_0 for the micropipe in (a).

We used the diameters D = 1.36 μm and D_0 = 1.82 μm to calculate the cross section area, 1.9 μm^2. Several sizes of the micropipes in our samples of 4*H*-SiC are shown in Table 1. In Table 2 we summarized the data of superscrew dislocation Burgers vector magnitudes b determined for the micropipes in 4*H*-SiC with a white SR topography [7], a transmission electron microscopy [8] and a polarized light microscopy [9].

Table 1 Micropipes parameters determined by the computer simulations. D is TD; D_0 is LD, and S is a cross section area

D, μm	D_0, μm	S, μm^2
1.80	0.50	0.7
4.10	0.40	1.3
1.44	1.68	1.9
1.82	1.74	2.5
1.70	2.05	2.7

Table 2 Surface energy γ and the superscrew dislocation Burgers vectors b [7-9]. S is calculated using the Frank formula [22]

γ, J m^{-2}	b	S, μm^2
0.2 [7, 8]	6*c*	0.6
	7*c*	1.2
	8*c*	2.1
0.94 [8]	12*c*	0.5
	17*c*	1.9
2 [9]	17*c*	0.4

By using the Frank formula: $D = \mu b^2 (4\pi^2 \gamma)^{-1}$ [22], which relates the diameter of an equilibrium micropipe D with its Burgers vector b, a shear modulus μ and a surface energy γ, one can estimate the diameter. However, this estimation needs some assumptions, because a precise value of γ is not available. In [7-9] the shear modulus was taken equal to μ = 200 GPa. The authors [8, 9] evaluated γ by using the correlation between b^2 and D. The values of the micropipe diameters differ between the data sources, as shown in Table 2. A remarkable discrepancy in γ values does not allow us any assumptions of the Burgers vector magnitudes of the micropipes in our 4*H*-SiC samples. We even do not know whether they are superscrew dislocations with open cores or not. Evidently the diameters measured by Ma [9] were much smaller than ours. In addition to quite big sizes and (sometimes) elliptical shapes, the other specific feature is described in the next section: we found that the section sizes changed along the micropipe axes.

4.2 Limitations of the one-dimensional computer simulations

The FIMTIM program determines two parameters of the elliptical intersection region of the micropipe by the x-ray beam: the one "across" (parallel to *x*, the diameter D) and the one "along" (parallel to *z*, the diameter D_0) the beam (Fig. 1(b)). However these values may not be equal to real diameters of the micropipe cross section, either circular or elliptical. A priori we do not know whether the micropipe axis is parallel to the sample surface or not; and in general

case it may have some angles with the coordinates shown in Fig. 1(b). One projection is not sufficient to restore the proper micropipe cross section. The analysis of possible angles [20] shows that the results of the simulation disagree with the real cross section sizes in the following cases.
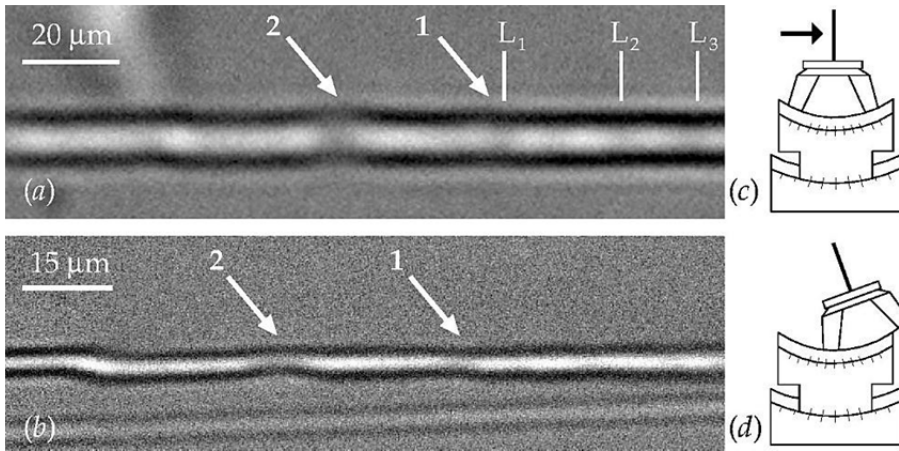
Fig. 3 SR phase-contrast images of a micropipe in SiC wafer. (a) The sample surface is fixed normal to the beam at a distance of 45 cm from the detector. (b) The sample is tilted 28° around the micropipe axis at a distance of 10 cm from the detector. Arrows 1 and 2 point to the regions of dark contrast. Lines L_1, L_2 and L_3 mark the simulated levels. (c) and (d) display the sample positions.

i. When a micropipe has an elliptical cross section and its axis is parallel to y (Fig. 1(b)) the major axis of the ellipse can have the angle Φ with x axis. Then the distances D and D_0 (across and along the beam) of the transmission function $T(x)$, given by (2), are not equal to the micropipe diameters d and d_0. The latter can be calculated from D and D_0 by means of the relation $D = [(d \cos\Phi)^2 + (d_0\sin\Phi)^2]^{1/2}$, $D_0 = d_0 d/D$ provided that the Φ angle is known. The Φ angle can be restored by fitting two projections measured for two different rotation angles around y axis.

ii. Let a micropipe have a circular cross section with diameter d, and let the micropipe axis have an angle $\theta < 90°$ with the beam direction (z in Fig. 1(b)). Such situation can take place when the micropipe is not parallel to the sample surface adjusted perpendicular to the beam. When θ is small, the image becomes dark in the center [23]. In this case the parameters of the transmission function can be expressed in d and θ as $D = d$ and $D_0 = d/\sin\theta$.

iii. Even if the micropipe axis is perpendicular to the beam, it can have an angle $\psi < 90°$ with the vertical plane (x, z) and hence the axis x in the plane (x, y) (Fig. 1(b)). In this case the parameters of the transmission function relate to the micropipe diameter d through the expression: $D = d/\sin\psi$ and $D_0 = d$. It is easy to correct the image position by rotating, but the source projection would increase to an unknown value and the precision of the simulation would decrease.

Our observations show that the micropipes can not only vary their orientation in space, but also their cross sections along their axes. Images of a micropipe with variable cross section are exemplified in Figs. 3(a) and 3(b). They were measured at the distances of 45 and 10 cm from a detector, respectively. In the top panel one can see that the contrast changes along the micropipe axis. In the regions marked by arrows 1 and 2, the central parts of the image darken up. The top panel shows the image for the perpendicular sample position sketched in Fig. 3(c). After tilting the sample by 28° around the axis perpendicular to the beam in the horizontal plane, as displayed in Fig. 3(d), we could see that the micropipe shape changed at the same levels 1 and 2 in Fig. 3(b). Fitting at the levels L_1, L_2 and L_3, marked by white lines in Fig. 3(a), confirmed the cross section change by giving the following diameters: $D = 1.05$ μm and $D_0 = 3.15$ μm at the level L_1; $D = 0.89$ μm and $D_0 = 3.70$ μm at the level L_2, and $D = 1.01$ μm and $D_0 = 2.44$ μm at the level L_3. At the same time, the cross section looked almost round between the levels L_1 and L_2: $D = 1.82$ μm and $D_0 = 1.74$ μm. The maps $\chi^2 - \chi^2_{min}$ (D, D_0) close to the minimum point had different shapes, but in all the cases the full minimum region was remarkably spreading.

We can now answer the question: can one trust the results of the simulation? Analysis compels us to prefer a negative reply. Indeed, the far field image in Fig. 3(a) is totally determined by the first Fresnel zone, and the distance between the edges is equal to $2r_1 = 2(\lambda z_1)^{1/2} = 11.8$ μm, where $\lambda = 0.775$ Å is the wavelength in the spectrum maximum (Fig. 1(a)) and $z_1 = 45$ cm. Meanwhile the distances between the levels L_1 - L_2 and L_2 - L_3 are 25 μm and 13.5 μm, respectively. Both the distances are comparable with $2r_1$. In the far field, the images are affected within the first Fresnel zone not only across but also along the micropipe axis. Even the most abrupt changes of the diameters are impossible to be detected in the one dimensional approach. Only the constant shape cross section keeps its proper size.

Concluding this section we notice that first, one dimensional approach restores the proper micropipe diameters only for the segments longer than $2r_1$ provided that they are constant in size and shape. Abrupt cross section changes are not detectable in the far field. Second, when the micropipe axis is in an arbitrary position relative to the beam, one cannot determine the diameters from only one projection. However, several projections might not be helpful either, since the micropipe position in the sample interior is beforehand unknown. In those cases when the image quickly changes along the micropipe axis, one deals with 2D rather than 1D object. In addition to the micropipes, crystals may contain other

voids which are spherical, capsule-like or faceted in shape. Their computer simulation needs 2D approach. The example will be given in the next section.
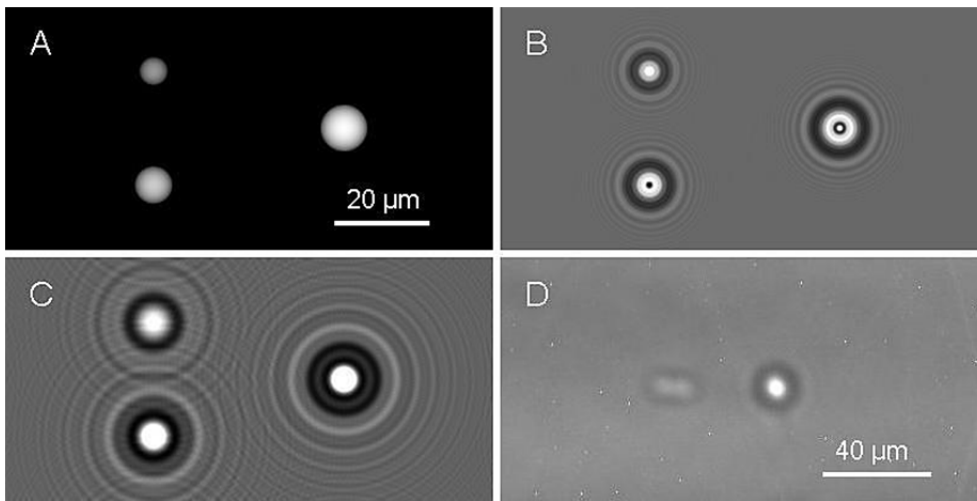
Fig. 4 (A) The map of thickness dependence for three spherical voids. (B) The calculated image of the voids at the distance 10 cm from the crystal. (C) The calculated image of the voids at the distance 50 cm. (D) The experimental image of one spherical void. The energy is 16 keV, the source-to-crystal distance is 34 m, and the crystal-to-detector distance is 45 cm. See text for details.

4.3 Computer simulation of spherical micro-voids in SiC crystal

Spherical micro-voids can be found in SiC crystals grown by sublimation. With growth, they usually develop into faceted voids, which provide information on the crystal habit and fast growth directions. Armed with this information, it would be easier to control the density of defects, which is particularly useful for the growth on nonstandard surfaces. It is of interest to know how the size of spherical micro-voids depends on growth parameters. Some spherical voids can be small and thus their phase contrast will be weak. Image measurements on various distances are therefore necessary even in the far field region. Because the sizes and structures of images are different, computer simulations of their images are useful to restore the diameters of such voids.

We have performed 2D computer simulations on the base of Eqs. (1) − (3), but in two dimensions. The same integral from the same propagator should be added with y coordinate and the transmission function $T(x,y)$ of the spherical void contains $(1 - (x^2 + y^2)/R^2)^{1/2}$ instead of $(1 - x^2/R^2)^{1/2}$ in the argument of exponential (phase factor). The 2D images can be shown similar to the experimental images as the grey level maps.

The 2D convolution of the Fresnel propagator and the transmission function is calculated on the finite set of points with numbers $N_1 * N_2$ and with the same step in both directions. As in the FIMTIM program, the method of Fast Fourier Transformation (FFT) is used. First, the Fourier image of $T(x,y)$ is calculated. The result $T(q,p)$ is obtained on the same set of points $N_1 * N_2$ in the reciprocal space, but with the various steps $\Delta q = 2\pi/(dN_1)$, $\Delta p = 2\pi/(dN_2)$. Then the reverse Fourier image of the product $T(q,p)P(q,Z)P(p,Z)$ is calculated on the same set of points. As a result, the square modulus of the wave function presents the image of the object on the set of points with the initial step in both directions. If necessary, the image can be convoluted with the Gaussian function to take into account the source size and the detector resolution.

Figure 4 shows the results of such simulations for the three spherical voids of various diameters 6, 8 and 10 μm. We used the 2048*1024 set of points with the step 0.05 μm. The monochromatic radiation is chosen with the photon energy 16 keV. The source-to-crystal distance is 34 m. The panel A shows the map of thickness of the voids in a matter, namely, $2R(1 - (x^2 + y^2)/R^2)^{1/2}$ together with the positions of the spherical voids. Here a black color corresponds to zero and a white color is for 10 μm.

The panel B shows the image (relative intensity) of the spherical voids at the distance 10 cm from the crystal. A point source and an ideal detector are assumed. Here a black color is used for 0.282 (minimum) and a white color for 2. The grey scale is linear. We note that the maximum of relative intensity is equal to 3.769 at the center of the right sphere, but all values more than 2 were replaced by 2 with the aim to show the background in the middle of grey scale. The image can be considered as an overexposed one. In reality very sharp peaks will be strongly smoothed by a convolution.

The panel C shows the images of the same objects at the distance 50 cm. Here a black color is used for 0.347 (minimum) and a white color for 2 again, but the maximum is equal to 6.695. We note that only the central regions of the right and bottom voids are overexposed. One can see that the diameters of the rings correspond to the Fresnel zone diameters which increase with the distance.

The panel D shows the fragment of experimental picture obtained with the monochromatic radiation 16 keV (multilayer monochromator) at the distance $z = 45$ cm from the crystal. For this distance the diameter of the first Fresnel zone $2(\lambda z)^{1/2} = 12$ μm. A comparison with the calculated images allows one to conclude that the diameter of the void is approximately 10 μm. The experimental image does not contain fine details because it is smoothed by the source size and the detector resolution.

5. Origin of oblate micropipes

To explain the reasons for deviations of the micropipe shape from the equilibrium cylindrical shape predicted by Frank [22], it is necessary to clearly understand the mechanisms and the stages of micropipes formation in the growing crystal. One possible scenario [24, 25] assigns a leading role to the coagulation of vacancies and includes the following main stages: (1) heterogeneous formation of dislocations elongated along the c axis and reaching the front of the crystal growth; (2) pipe diffusion of vacancies from the surface into the crystal bulk through the cores of these dislocations; (3) coagulation of these vacancies around the dislocation lines; (4) forming a continuous cavity (micropipe) around dislocations and leveling its surface by surface diffusion of vacancies. Under this scenario of micropipe formation, many of the features of their morphology, which are often observed in the experiment, become clear: (1) the instability of micropipe diameter, (2) the instability of its cylindrical shape, (3) the local curvature of micropipes, (4) the formation on the micropipes of large drop-like pores whose cross-section size is much larger than the cross-section size of the micropipes, (5) sudden breaks of micropipes, *etc*. Indeed, diffusion, coagulation and subsequent absorption-emission of vacancies by micropipes are strongly nonequilibrium processes, so that the micropipe formation can be determined by the process kinetics rather than by Frank's thermodynamics [22].

Consider now how one can use this scheme to explain the formation of oblate micropipes. Take more than one, as before, but a few dislocations that originated on one source (a large surface step, a pore, an inclusion of other material or foreign SiC polytype, *etc*.). In the simplest case, this can be a dislocation dipole or a pair of dislocations of the same sign. If these dislocations are located not too far from each other, then, during the vacancy coagulation, the newly generated micropipe can capture both the dislocations and immediately purchase at this a section elongated in the direction from one dislocation to the other. Divergence or convergence of dislocations in the crystal growth will cause a corresponding change in the cross section of such an oblate micropipe, while deviations of the dislocations in the directions at an angle to the imaginary line connecting them or, even more so, twisting of the dislocations around a common axis will be observed as twisting of the oblate micropipe.

Let us estimate the conditions under which the formation of such oblate micropipes is energetically favorable. In the case of dislocation dipole, a micropipe comprising both the dislocations has the distinct advantage that the dislocations annihilate inside the micropipe. Therefore, there is a gain in the dislocation strain energy and the dislocation core energy. At the same time, an increase in the micropipe volume, required to comprise the entire dipole, leads to corresponding increase in the energy of the micropipe free surface. The energy balance determines a critical size of the micropipe, which it cannot exceed. In the initial state (before the micropipe formation), the total energy of the dislocation dipole per its unit length is $W_1 = Gb^2/(2\pi)[\ln(d/r_c) + 2Z]$, where G is the shear modulus, b is the Burgers vector magnitude, d is the dipole arm (equal to TD at the certain level along the micropipe axis), r_c is the cut-off radius of the dislocation elastic fields on its core, and $Z \approx 1$ is the dimensionless parameter characterizing the dislocation core energy. After the micropipe formation and dipole annihilation, the total energy of the system per unit length of annihilated dislocations can be estimated as $W_2 = \gamma L$, where γ is the specific energy of the crystal free surface and L is the average perimeter of the micropipe cross section. The micropipe formation is energetically favorable if the corresponding energy change is negative: $\Delta W_{dd} = W_2 - W_1 = \gamma L - Gb^2/(2\pi)[\ln(d/r_c) + 2Z] < 0$. From this inequality, we get at once a limitation for L: $L < L_c = Gb^2/(2\pi\gamma)[\ln(d/r_c)+2Z]$, where L_c is a critical perimeter of the micropipe cross section.

The dependence of the energy change ΔW_{dd} on the dipole arm d is shown in Fig. 5(a) for the parameter values taken for 4*H*-SiC: $c = 1$ nm, $G = 165$ GPa, and $\gamma = 0.2$ Jm^{-2} [26]. The curves $\Delta W_{dd}(d)$ are built for three values of the Burgers vector: $b = nc$ with $n = 1$, 2 and 3. The cut-off radius was taken equal to the Burgers vector magnitude: $r_c = b$. In calculations, we assumed that the micropipe cross-section perimeter L is in direct proportion with the dipole arm d: $L = \eta d$ with $\eta = 2.5$ (the lowest value of η, $\eta \approx 2$, corresponds to a flat slit, while its highest value $\eta \approx \pi$ corresponds to a circle). As is seen from Fig. 5(a), the maximum energy gain is reached at $d \approx 0.07$, 0.21 and 0.47 μm for $n = 1$, 2 and 3, respectively. At the same time, the micropipe formation remains energetically favourable for much larger values of d, until $d < d_c = L_c/2.5 \approx 0.40$, 1.82 and 4.40 μm for $n = 1$, 2, and 3, respectively. Oblate micropipes of such transverse diameters are often observed in our experiments.
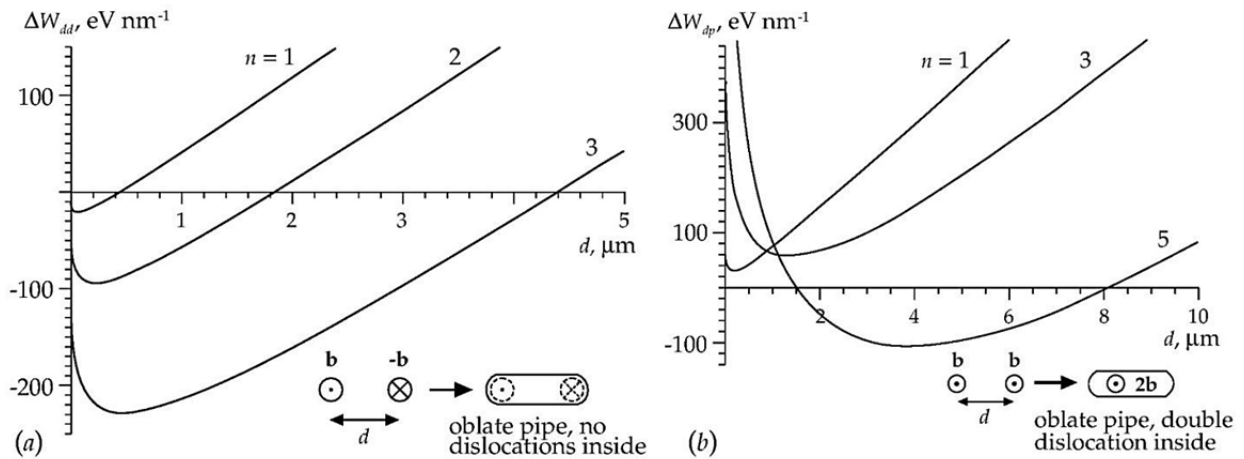
Fig. 5 (a) Dependence of the energy change ΔW_{dd} on the dislocation dipole arm d for $b = nc$ ($n = 1$, 2 and 3) at $c = 1$ nm, $G = 165$ GPa, $\gamma = 0.2$ J m^{-2} and $\eta = 2.5$. The inset shows a scheme of the dipole annihilation after an oblate micropipe has formed around it. (b) Dependence of the energy change ΔW_{dp} on the dislocation spacing d for $b = nc$ ($n = 1$, 3 and 5) $c = 1$ nm, $G = 165$ GPa, $\gamma = 0.2$ J m^{-2} and $\eta = 2.5$. The inset shows a scheme of the dislocation agglomeration after an oblate micropipe has formed around a dislocation pair.

In the case when an oblate micropipe forms around a pair of dislocations of the same sign, the similar energy terms read: $W_1 = Gb^2/(2\pi)[\ln\{R^2/(dr_c)\} + 2Z]$ and $W_2 \approx \gamma L + 2Gb^2/\pi \ln(2R/d)$. Therefore, the energy change due to the micropipe formation is $\Delta W_{dp} = W_2 - W_1 = \gamma L + Gb^2/(2\pi)[\ln(16R^2r_c/d^3) - 2Z]$, where R is the parameter of screening the long-range elastic dislocation fields. We can estimate it as a half of the average distance between dislocations of opposite signs in the crystal. In our calculations, we used the value of $R = 10$ μm which corresponds to the dislocation density $\sim 10^6$ cm^{-2} typical for regions of dislocation generation in our samples.

The dependence of the energy change ΔW_{dp} on the dislocation spacing d is shown in Fig. 5(b) for the same values of the system parameters as before. The curves $\Delta W_{dp}(d)$ are built for three values of the Burgers vector: $b = nc$ with $n = 1$, 3 and 5. It is seen from Fig. 5(b) that the formation of an oblate micropipe around a pair of identical dislocations with Burgers vectors of magnitude $1c$ and $3c$ is not energetically favorable. To form such a micropipe, the Burgers vector magnitude must not be smaller than $5c$. At $b = 5c$, the micropipe size can vary from approximately 1.5 to 8.2 μm, and the maximum profit in the energy is for $d \approx 4$ μm. Thus, in contrast with the previous case of a dislocation dipole, when the oblate micropipe formation is energetically favorable for any magnitude of the Burgers vector and for $d < d_c$, here we have got two critical conditions for the oblate micropipe formation: $b \geq b_c = 5c$ and $d_{c1} < d < d_{c2}$. The interval of acceptable values of d is determined by the Burgers vector magnitude: the larger b the wider this interval.

Summarizing the above discussion, the formation of oblate micropipes can be explained by their trend to comprise some dislocations (dislocation bundle) at once with minimizing the micropipe surface. The largest size of the micropipe cross section is then approximately equal to the distance between the farthest dislocations in the bundle. If the dislocation bundle is a self-screened ensemble of dislocations, from a dipole to an arbitrary multipole, then the driving force of the dislocation agglomeration inside one micropipe is total annihilation of dislocations there, while the main limitation of such agglomeration is that the bundle size cannot be larger than its critical size d_c. If the dislocation bundle consists of dislocations of the same sign (or of opposite signs but when the number of dislocations of one sign differs from the number of dislocations of the opposite sign), then the driving force of the dislocation agglomeration within one micropipe is a decrease in the strain energy density near the bundle. The main limitations in this case are that (1) the Burgers vector magnitudes of the residual dislocations must be larger than a critical value b_c and (2) the transverse size of the bundle of residual dislocations (the largest distance between them) must be in the range between two critical values d_{c1} and d_{c2}, which is determined by the value of b. Our numerical estimates of critical values d_c, d_{c1} and d_{c2} are in good accordance with the sizes of oblate micropipes observed in our experiments.

6. Concluding remarks

Computer simulations are necessary to determine micro-object sizes and shapes from their phase contrast images recorded in the far field. Micropipes in SiC crystals are particular phase objects having small cross section sizes along the beam. Under Fraunhofer diffraction conditions the central part of the micropipe image is determined by the product DD_0, hence by the cross section area, rather than by the diameters D and D_0 across and along the beam. A broad spectrum of the pink SR beam weakly influences the central image part but leads to damping the oscillations, so only the first oscillations remain on each side. That is why it is useful to analyze the map of least square sum χ^2 as a

function of D and D_0, which allows one to estimate the accuracy of the diameters restoring. We have discovered that the map demonstrates a weak localization of the area of small χ^2.

The 1D simulation approach allows us to restore only those micropipe cross sections which are constant in size and shape along the axes. By using a 2D approach these limitations are removed. Of course, the use of pink beam experimental data is not the best for the both 1D and 2D simulations. Another option is the use of a low monochromaticity SR beam (for example, with $\Delta E/E = 10^{-1}$) that provides a sufficient temporal coherence length with a reasonably high intensity.

The origin of oblate micropipes can be a result of enhanced diffusion of vacancies along dislocation cores with their consequent coalescence and transformation into oblate micropipes comprising at once some dislocations (dislocation bundles) with minimizing the micropipe surface.

References

[1] Hwu Y, Hsieh H, Lu M-J, Tsai WL, Lin HM, Goh WC, Lai B, Je JH, Kim CK, Noh DY, Youn HS, Tromba G, Margaritondo G. Coherence-enhanced synchrotron radiology: refraction versus diffraction mechanisms. J. Appl. Phys. 1999; 86:4613-18.

[2] Kohn VG, Argunova TS, Je JH. Study of micropipe structure in SiC by x-ray phase contrast imaging. Appl. Phys. Let. 2007; 91: 171901.

[3] Mayo SC, Stevenson AW, Wilkins SW. In-line phase-contrast x-ray imaging and tomography for materials science. Materials 2012; 5:937-65.

[4] Gutkin MYu, Sheinerman AG, Argunova TS, Mokhov EN, Je JH, Hwu Y, Tsai WL, Margaritondo G. Micropipe evolution in silicon carbide. Appl. Phys. Lett. 2003; 83:2157-59.

[5] Gutkin MYu, Sheinerman AG, Smirnov MA, Kohn VG, Argunova TS, Je JH, Jung JW. Correlated reduction in micropipe cross sections in SiC growth. Appl. Phys. Lett. 2008; 93: 151905.

[6] Argunova TS, Gutkin MYu, Kostina LS, Grekhov IV, Belyakova EI, Je JH. Crack-free interface in wafer-bonded Ge/Si by patterned grooves. Scripta Mater 2010; 62:407-10.

[7] Huang XR, Dudley M, Vetter WM, Huang W, Wang SC, Carter CH, Jr. Direct evidence of micropipe-related pure superscrew dislocations in SiC. Appl Phys. Lett. 1999; 74:353-55.

[8] Strunk HP, Dorsch W, Heindl J. The nature of micropipes in 6H-SiC single crystals. Adv. Eng. Mater. 2000; 2:386-389.

[9] Ma X. A method to determine superscrew dislocation structure in silicon carbide. Mater. Sci. Eng. B 2006; 129:216-21.

[10] Born M, Wolf E. Principles of optics. 4-th Ed. Pergamon Press, 1968, chapter 10.

[11] Afanas'ev AM, Kon VG. On the coherence length of x rays. Sov. Phys. Crystallogr. 1977; 22:355.

[12] Vodakov YuA, Roenkov AD, Ramm MG, Mokhov EN, Makarov YuN. Use of Ta-container for sublimation growth and doping of SiC bulk crystals and epitaxial layers. Phys. Status Solidi B 1997; 202:177-00.

[13] Snigirev A, Snigireva I, Kohn V, Kuznetsov S, Schelokov I. On the possibilities of x-ray phase contrast microimaging by coherent high-energy synchrotron radiation. Rev. Sci. Instrum. 1995; 66:5486-92.

[14] Kohn VG, Argunova TS, Je JH. Far-field x-ray phase contrast imaging has no detailed information on the object. J. Phys. D: Appl. Phys. 2010; 43:442002.

[15] Kohn VG, Argunova TS, Je JH. Features in phase-contrast images of micropipes in SiC in white synchrotron radiation beam. J. Surf. Investig. 2011; 5:1-6.

[16] Cowley JM. Diffraction Physics, 3-d Ed., Elsevier, Amsterdam, 1995.

[17] Argunova TS, Kohn VG, Je JH. Computer simulation of phase-contrast images in white synchrotron radiation using micropipes in Silicon Carbide. J. Surf. Investig. 2008; 2:861-65.

[18] Argunova T, Kohn V, Jung J-W, Je J-H. Elliptical micropipes in SiC revealed by computer simulating phase contrast images. Phys. Status Solidi A 2009; 206:1833-37.

[19] Kohn VG. Focusing femtosecond x-ray free-electron laser pulses by refractive lenses, J. Synchr. Rad. 2012; 19; 84-92.

[20] Kohn VG, Argunova TS, Je JH. Quantitative hard x-ray phase contrast imaging of micropipes in SiC. AIP Advances 2013; 3:122109.

[21] The program can be freely downloaded at http://imagej.nih.gov/ij/download.html

[22] Frank FC. Capillary equilibria of dislocated crystals. Acta Crystallogr. 1951; 4:497-501.

[23] Kohn VG, Argunova TS, Je JH. On the cause of a contrast change in the SR images of micropipes in SiC. J. Surf. Investig. 2012; 6: 840-44.

[24] Argunova TS, Gutkin MYu, Je JH, Kohn VG, Mokhov EN. Characterization of defect evolution in bulk SiC by synchrotron x-rays imaging, In: Physics and Technology of Silicon Carbide Devices, Ed. by Y. Hijikata, Section 1, Chapter 2, InTech, Croatia, 2013, p. 27–45.

[25] Argunova TS, Gutkin MYu, Je JH, Lim JH, Mokhov EN, Roenkov AD. Structural transformation of lattice defects in free-spreading growth of bulk SiC crystals. CrystEngComm 2014, submitted.

[26] Si W, Dudley M, Glass R, Tsvetkov V, Carter Jr. C. Hollow-core screw dislocations in 6H-SiC single crystals: A test of Frank's theory. J. Electron. Maters. 1997; 26:128–133.